KSCE Journal of Civil Engineering
DOI 10.1007/s12205-024-1319-6

pISSN 1226-7988, eISSN 1976-3808
www.springer.com/12205

Structural Engineering

Analysis of Strain Transfer Efficiency Coefficient of a Novel High-strength Steel Wire FBG Sensor

Kun Yan[a,b], **Zhixiong Yi**[a], **Qi Li**[a,b], **Gang Liu**[c], **Chaoyue Jiang**[a,b], **and Lu Wang**[d]

[a]*China Merchants Chongqing Communications Technology Research & Design Institute Co., Ltd., Chongqing 400067, China*
[b]*State Key Laboratory of Bridge Engineering Safety and Resilience, Chongqing 400067, China*
[c]*School of Civil Engineering, Chongqing University, Chongqing 400044, China*
[d]*School of Civil Engineering and Architecture, Southwest University of Science and Technology, Mianyang 621010, China*

ARTICLE HISTORY

Received 27 June 2023
Revised 25 April 2024
Accepted 7 May 2024
Published Online 13 July 2024

KEYWORDS

Bridge cables
Parallel steel wire
High-strength steel wire FBG sensor
Strain transfer efficiency coefficient
Theoretical formula
Finite element simulation
Experiments

ABSTRACT

Accurately measuring cable forces is crucial for reliable bridge condition evaluation, yet it remains a challenging task. This study proposes the use of a High-strength Steel Wire Fiber Bragg Grating (HSW-FBG) sensor embedded in commonly-used cables composed of 5 – 7 mm parallel steel wires. The HSW-FBG sensor facilitates direct strain measurement, offering a simple and user-friendly packaging process for high-precision monitoring throughout the cable's lifespan. The results demonstrate excellent linearity and repeatability in strain detection of the HSW-FBG sensor. The length of the packaging layer has the most significant impact on the strain transfer efficiency (STE) coefficient and should be at least 60 mm required for optimal performance. Additionally, the elastic modulus of the packaging layer moderately affects the STE coefficient. Adhering to these packaging parameter requirements ensures that the STE coefficient of the HSW-FBG sensor is very close to 1, enabling for high-precision measurement without correction. A systematic analysis of the STE coefficient of the HSW-FBG sensor is conducted, determining reasonable values for the packaging parameters. These findings lay the groundwork for future engineering applications, facilitating accurate measurement of cable forces in practical scenarios.

1. Introduction

Bridge cables are critical load-bearing components of long-span bridges, but they encounter challenges such as high operational stress, harsh environmental conditions, and limited replaceability and maintainability. Over time, factors like fatigue and corrosion of the steel wire can deteriorate the performance and service life of the cables (Wang et al., 2021a). Therefore, monitoring the cable's condition, including cable force and stress history, is vital for cable maintenance. Several methods are employed to measure cable force, including the vibration frequency method (Kangas et al., 2012), magnetic flux method (Wang et al., 1999), microwave radar method (Camassa et al., 2021; Weng et al., 2023), laser scanning method (Mehrabi and Farhangdoust, 2018; Zhou et al., 2021), and multiple digital images method (Jo et al., 2021). Intelligent cables equipped with sensors can also be used to monitor cable force or steel wire stress (Zhao et al., 2013; Wang et al., 2021b). The packaging process of sensors in intelligent cables typically involves: 1) affixing the sensor using clamps onto the outermost wire of the strand (Liu et al., 2010); 2) embedding the sensors in the cable's anchor head (Wu et al., 2012); 3) manufacturing fiber reinforced plastic-optical fiber Bragg grating (FRP-OFBG) (Li et al., 2009; Li et al., 2011; Kalamkarov et al., 2000; Kulpa et al., 2021) and basalt fiber reinforced polymer-fiber Bragg grating (BFRP-FBG) (Wu et al., 2022) composite wires, embedding them along the entire cable length. However, these methods primarily focus on measuring axial force or stress of the cable. Due to the cable's bending stress and uneven stress distribution across the steel wires, these methods cannot adequately monitor the time-history stress of individual steel wires, which is crucial for analyzing the cable's fatigue performance.

The theoretical research and practical applications of Fiber Bragg Grating (FBG) have gained significant attention in the field of optical research ever since its creation by Hill et al.

CORRESPONDENCE Lu Wang ✉ wanglu_bridge@163.com School of Civil Engineering and Architecture, Southwest University of Science and Technology, Mianyang 621010, China

(1978). FBG sensors exhibit several desirable characteristics, including a small diameter, high durability, precise measurement accuracy, and excellent reliability (Ren et al., 2014). The sensor have found successful applications in various fields, such as the natural gas and oil industry, civil engineering structures, and offshore engineering structures (Majumder et al., 2008; Yun and Min, 2011; Vosoughifar et al., 2019; Sahota et al., 2020), where they are used to monitore relative strains (Im et al., 2014), deformation (Mueller et al., 2006; Hou et al., 2021; Bonopera, 2022), forces (Yao et al., 2021), temperatures (Mahakud et al., 2013), fractures (Yashiro et al., 2007) and vibrations (Salo and Korhonen, 2014). The versatility and effectiveness of FBG sensors have positioned them a valuable tool in many industries and research domains.

Packaging sensors on high-strength steel wires in bridge cables, which typically feature numerous parallel steel wires with diameters ranging from 5 to 7 mm, poses significant challenges. Chen et al. (2012) proposed using metals such as lead, aluminum, zinc, and nickel with higher elastic moduli for packaging FBG sensors on high-strength steel wires. However, the metallized packaging process is complex, and the packaging layer exhibits poor adhesion to the steel wire, resulting in inadequate anti-fatigue performance and unsuitability for accurately measuring large strain in the steel wire. Another drawback of metallized fiber grating sensors is their relatively low strain transfer efficiency (STE) coefficient, necessitating correction of the strain measured by the FBG sensor during application. Given these limitations, the metallized packaging approach is not suitable for long-term strain monitoring of the steel wires. For FBG sensors packaged in tubular or substrate forms, it is recommended to use packaging materials with higher elastic moduli, and the detected strain of the sensors should be corrected (Zhang et al., 2016), as the packaging length cannot be excessively large.

In consideration of the high slenderness ratio of both high-strength steel wire and FBG, a novel approach is proposed to directly package the bare FBG sensor on the surface of the steel wire along the length of the cable. This innovative approach results in the creation of the High-strength Steel Wire FBG (HSW-FBG) sensor, which serves as both a force-bearing component of the cable and a stress measurement sensor for the steel wire, as depicted in Fig. 1. The packaging technology employed for the HSW-FBG sensor is crucial in ensuring its durability, reliability, and measurement precision.

For the HSW-FBG sensor with local surface packaging, the STE coefficient plays a significant role in accurate strain measurement. Additionally, the choice of packaging materials, dimensions (Chen et al., 2012; Di Sante et al., 2014; Zeng et al., 2019), and packaging methods (Li et al., 2007; Torres et al., 2011) may greatly influence the STE coefficient. Consequently, it is essential to conduct a comprehensive study on the STE coefficient of the HSW-FBG sensor and determine optimal packaging parameters.

This study employs a combination of theoretical formula derivation, finite element simulation, and experimental analysis to investigate the calculation formula of the STE coefficient for the HSW-FBG sensor, as well as its influential parameters. Additionally, suitable package dimension parameters are determined. These findings provide a robust foundation for the application of intelligent cables.

2. Derivation of Theoretical Formula

The FBG sensor comprises an optical fiber core, optical fiber cladding, and coating. Once packaged as an HSW-FBG sensor, it becomes integrated with the high-strength steel wire through the packaging layer. The cross-section of the HSW-FBG sensor is illustrated in Fig. 2. When axial tension is applied to the steel wire, the resulting strain is transmitted to the optical fiber through the packaging layer, enabling measurement by the FBG sensor. However, due to the shear deformation of the FBG and packaging materials during the strain transfer process, the axial strain of the steel wire is not fully transferred to the FBG sensor. Consequently, the ratio between the strain detected by the sensor and the strain of steel wire, known as the STE coefficient, is always less than 1 (Ansari and Libo, 1998). In the theoretical analysis of the strain transfer in the HSW-FBG sensor, a simplified four-layer structure model is employed, comprising the steel wire layer, packaging layer, coating layer, and optical fiber layer. Based on the shear-lag theory, a mechanical model for strain

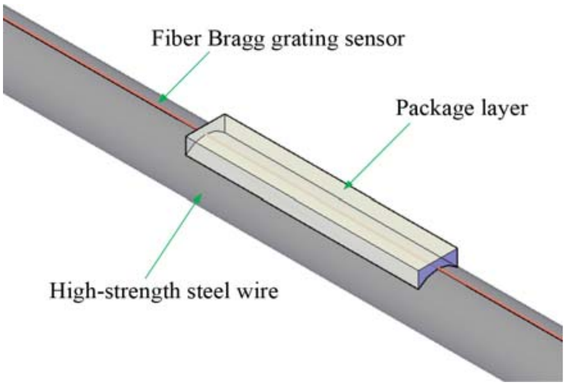

Fig. 1. Schematic Diagram of the HSW-FBG Sensor

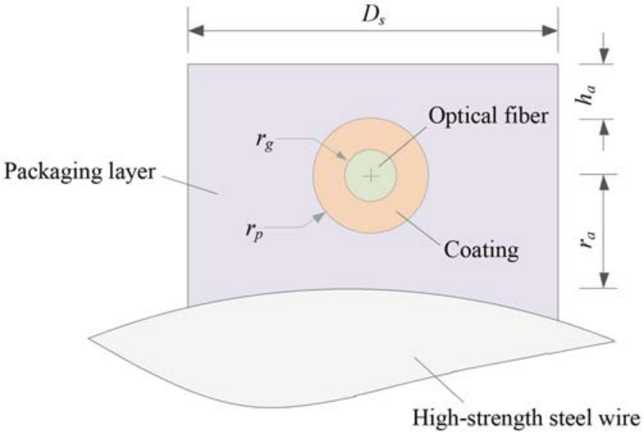

Fig. 2. Cross Section of HSW-FBG Sensor

transfer is established, and the formula for the STE coefficient is derived. Additionally, the optimal size of the packaging layer is determined.

2.1 Basic Assumptions

To accurately calculate the STE coefficient for the HSW-FBG sensor, it is important to consider the geometric and physical characteristics, as well as the interface stress characteristics, of the FBG, packaging materials, and steel wire. To simplify the analysis while still capture the essential characteristics of the strain transfer mechanism in the HSW-FBG sensor, the following three assumptions are adopted:

1. The axial strain at the surface of the steel wire is assumed to be equivalent to that at the center, neglecting the slight bending effect caused by the packaging layer.
2. The shear stress is assumed to vary in an approximately linearly fashion across the thickness direction within the packaging layer, optical fiber layer, and coating layer.
3. The interfaces between the optical fiber, coating layer, packaging layer, and steel wire are assumed to be perfectly bonded, and there is no relative slip at these interfaces during the loading process.

2.2 Strain Transfer Theory of FBG Sensor

The micro-segment stress diagram of HSW-FBG sensor is shown in Fig. 3. The coordinate origin is located at the midpoint of the packaging layer, i.e., the midpoint of fiber Grating. $\sigma(x, r)$ and $\tau(x, r)$ are the normal stress and shear stress on the section of each micro-segment, respectively.

2.2.1 Mechanical Properties of Optical Fiber, Coating and Packaging Layer

First, the mechanical balance equations of the optical fiber, coating, and packaging layer microsegments can be derived as follows:

$$\pi r_g{}^2\sigma_g = \pi r_g{}^2(\sigma_g + d\sigma_g) + 2\pi r_g dx\tau(x, r_g)\ , \tag{1}$$

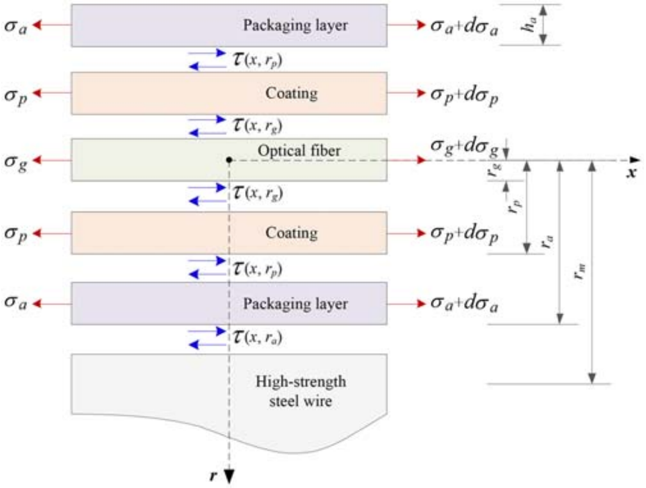

Fig. 3. Schematic Diagram of Micro-Segment Stress of HSW-FBG Sensor

$$\sigma_p\pi(r_p{}^2 - r_g{}^2) + \tau(x, r_g)2\pi r_g = (\sigma_p + d\sigma_p)\pi(r_p{}^2 - r_g{}^2) + \tau(x, r_p)2\pi r_p\ , \tag{2}$$

$$\begin{aligned}&\sigma_a[D_a(h_a + r_p + r_a) - \pi r_p{}^2] + \tau(x, r_p)2\pi r_p dx \\ &\quad = (\sigma_a + d\sigma_a)[D_a(h_a + r_p + r_a) - \pi r_p{}^2] + \tau(x, r_a)D_a dx,\end{aligned} \tag{3}$$

where D_a, h_a and $r_a - r_p$ are the width, upper thickness and lower thickness of the package layer, respectively; E, G and λ are the elastic modulus, shear modulus and Poisson's ratio of each layer of material, respectively; x and r represent the location of each microsegment along the axial and radial direction, respectively; The subscripts g, p, a and m denote the optical fiber layer, coating layer, packaging layer and base layer, respectively.

From Eqs. (1) – (3), the stress differential equations of the optical fiber, coating and packaging layers can be obtained:

$$\frac{d\sigma_g}{dx} = -2\frac{\tau(x, r_g)}{r_g}\ , \tag{4}$$

$$\frac{d\sigma_p}{dx} = \frac{2[r_g\tau(x, r_g) - r_p\tau(x, r_p)]}{r_p{}^2 - r_g{}^2}\ , \tag{5}$$

$$\frac{d\sigma_a}{dx} = \frac{2\pi r_p\tau(x, r_p) - \tau(x, r_a)D_a}{D_a(h_a + r_p + r_a) - \pi r_p{}^2}\ . \tag{6}$$

According to Eqs. (4) and (5):

$$\tau(x, r_p) = -2\frac{r_g{}^2}{r_p}\frac{d\sigma_g}{dx} - (\frac{r_p}{2} - \frac{r_g{}^2}{2r_p})\frac{d\sigma_p}{dx}\ . \tag{7}$$

According to Eqs. (6) and (7):

$$\tau(x, r_a) = -\frac{4\pi r_g{}^2}{D_a}\frac{d\sigma_g}{dx} - \frac{\pi(r_p{}^2 - r_g{}^2)}{D_a}\frac{d\sigma_p}{dx} - (h_a + r_p + r_a - \frac{\pi r_p{}^2}{D_a})\frac{d\sigma_a}{dx}\ . \tag{8}$$

Recalling the assumption (2), Eqs. (7) and (8) can be combined as:

$$\tau(x, r) = \begin{cases} -2\dfrac{r_g{}^2}{r}\dfrac{d\sigma_g}{dx} - (\dfrac{r}{2} - \dfrac{r_g{}^2}{2r})\dfrac{d\sigma_p}{dx} & r_g < r < r_p \\ -\dfrac{4\pi r_g{}^2}{D_a}\dfrac{d\sigma_g}{dx} - \dfrac{\pi(r_p{}^2 - r_g{}^2)}{D_a}\dfrac{d\sigma_p}{dx} - (h_a + r_p + r - \dfrac{\pi r_p{}^2}{D_a})\dfrac{d\sigma_a}{dx} & r_p < r < r_a\ . \end{cases} \tag{9}$$

Then, substituting the stress-strain relationship $\sigma = E\varepsilon$ into Eq. (9) gives:

$$\tau(x, r) = \begin{cases} -2\dfrac{r_g{}^2}{r}E_g\dfrac{d\varepsilon_g}{dx} - (\dfrac{r}{2} - \dfrac{r_g{}^2}{2r})E_p\dfrac{d\varepsilon_p}{dx} & r_g < r < r_p \\ -\dfrac{4\pi r_g{}^2}{D_a}E_g\dfrac{d\varepsilon_g}{dx} - \dfrac{\pi(r_p{}^2 - r_g{}^2)}{D_a}E_p\dfrac{d\varepsilon_p}{dx} - (h_a + r_p + r - \dfrac{\pi r_p{}^2}{D_a})E_a\dfrac{d\varepsilon_a}{dx} & r_p < r < r_a\ . \end{cases} \tag{10}$$

According to the assumption 3, the strain coordination and deformation continuity between the interfaces are maintained during the strain transfer process, so the strain gradient at each interface are assumed to be approximately equal:

$$\frac{d\varepsilon_g}{dx} \cong \frac{d\varepsilon_p}{dx} \cong \frac{d\varepsilon_a}{dx} \cong \frac{d\varepsilon_m}{dx}\ . \tag{11}$$

Substituting Eqs. (11) into Eq. (10) gives:

$$\tau(x,r)=\begin{cases} -[2\frac{r_g{}^2}{r}E_g+(\frac{r}{2}-\frac{r_g{}^2}{2r})E_p]\frac{d\varepsilon_g}{dx} & r_g<r<r_p \\ -[\frac{4\pi r_g{}^2}{D_a}E_g+\frac{\pi(r_p{}^2-r_g{}^2)}{D_a}E_p+(h_a+r_p+r-\frac{\pi r_p{}^2}{D_a})E_a]\frac{d\varepsilon_g}{dx} & r_p<r<r_a. \end{cases} \tag{12}$$

According to the assumption 2, that is:

$$\tau(x,r)=\begin{cases} G_p\gamma(x,r)=G_p(\frac{\partial u}{\partial r}+\frac{\partial w}{\partial x})\cong G_p\frac{\partial u}{\partial r} & r_g<r<r_p \\ G_a\frac{\partial u}{\partial r} & r_p<r<r_a, \end{cases} \tag{13}$$

where u is the axial displacement; w is the radial displacement; $G_p=E_p/[2(1+\lambda_p)]$ and λ_p are the shear modulus and Poisson's ratio of the coating layer, respectively.

Substitute Eqs. (13) into Eq. (12), and integrate (r_g, r_p) and (r_p, r_a) respectively, it can be obtained as:

$$u_a-u_g=-\frac{1}{k_1^2}\frac{d\varepsilon_g}{dx}, \tag{14}$$

where,

$$k_1=\sqrt{\frac{1}{k_gE_g+k_pE_p+k_aE_a}}, \tag{15}$$

$$k_g=\frac{2r_g{}^2}{G_p}\ln\frac{r_p}{r_g}+\frac{(r_a-r_p)4\pi r_g{}^2}{G_aD_a}, \tag{16}$$

$$k_p=\frac{(r_p{}^2-r_g{}^2)}{4G_p}-\frac{r_g{}^2}{2G_p}\ln\frac{r_p}{r_g}+\frac{\pi(r_p{}^2-r_g{}^2)(r_a-r_p)}{G_aD_a}, \tag{17}$$

$$k_a=\frac{(h_a+\frac{3}{2}r_p+\frac{1}{2}r_a-\frac{\pi r_p{}^2}{D_a})(r_a-r_p)}{G_a}. \tag{18}$$

The derivation of x on both sides of Eq. (14) is reduced to:

$$\frac{d^2\varepsilon_g(x)}{dx^2}+k_1{}^2\varepsilon_a-k_1{}^2\varepsilon_g=0. \tag{19}$$

The general solution of Eq. (19) is:

$$\varepsilon_g(x)=c_1e^{k_1x}+c_2e^{-k_1x}+\varepsilon_a \tag{20}$$

The length of the packaging layer is $2L$. According to the free end face of the packaging layer and its symmetry, the boundary conditions are:

$$\begin{cases} \varepsilon_g(L)=\varepsilon_g(-L)=0 \\ \dot{\varepsilon}_g(0)=0. \end{cases} \tag{21}$$

Substitute Eqs. (18) into (20) and solve the integral constant to obtain:

$$\varepsilon_g(x)=\varepsilon_a\left[1-\frac{\cosh(k_1x)}{\cosh(k_1L)}\right], \tag{22}$$

where $\varepsilon_g(x)$ is the axial strain of the optical fiber, and ε_a is the strain at the interface between the packaging layer and the steel wire.

According to Eq. (12), the shear strain expression at the interface between the packaging layer and the steel wire is:

$$\tau(x,r_a)=\frac{E_{eq}k\varepsilon_a\sinh(k_1x)}{\cosh(k_1L)}. \tag{23}$$

where:

$$E_{eq}=\frac{4\pi r_g{}^2}{D_a}E_g+\frac{\pi(r_p{}^2-r_g{}^2)}{D_a}E_p+(h_a+r_p+r_a-\frac{\pi r_p{}^2}{D_a})E_a. \tag{24}$$

2.2.2 Mechanical Properties of High-Strength Steel Wire

Similarly, the microsegment with radius r_a to r_m ($r_a<r<r_m$) is considered for the following stress analysis.

$$\frac{d\sigma_m}{dx}=\frac{\tau(x,r_a)}{r_m-r_a} \tag{25}$$

Substitute the stress-strain relationship $\sigma=E\varepsilon$ into Eq. (25) and combine Eq. (23) to obtain:

$$\frac{d\sigma_m}{dx}=\frac{E_{eq}k\varepsilon_a\sinh(k_1x)}{E_m(r_m-r_a)\cosh(k_1L)}. \tag{26}$$

The expression of the influence depth of sensor on steel wire is obtained by combining Eqs. (11), (22) and (26):

$$r_m-r_a=\frac{E_{eq}}{E_m}. \tag{27}$$

According to the assumptions, shear stress varies linearly along the thickness direction within the range of influence depth of steel wire, and the shear stress meets the boundary conditions:

$$\tau(x,r)=\begin{cases} \tau(x,r_a) & r=r_a \\ 0 & r=r_m. \end{cases} \tag{28}$$

From the above derivation, the shear stress within the influence depth of steel wire can be expressed as:

$$\tau(x,r)=\frac{\tau(x,r_a)}{r_m-r_a}(r_m-r) \qquad r_a<r<r_m. \tag{29}$$

Substitute $\tau=G\frac{du}{dr}$ into Eq. (29), and integrate r on both sides, then substitute the second formula of Eq. (12), and finally combine Eq. (14) to get:

$$u_m-u_g=-\frac{1}{k^2}\frac{d\varepsilon_g}{dx}, \tag{30}$$

where:

$$k=\sqrt{\frac{1}{\frac{1}{k_1^2}+\frac{E_{eq}}{2G_m}}}. \tag{31}$$

The derivative of x on both sides of Eq. (30) is:

$$\frac{d^2\varepsilon_g(x)}{dx^2}-k^2\varepsilon_g+k^2\varepsilon_m=0. \tag{32}$$

The general solution of Eq. (32) is:

$$\varepsilon_g(x) = c_3 e^{kx} + c_4 e^{-kx} + \varepsilon_m \qquad -L \le x \le L\ . \tag{33}$$

According to the free state of fiber end and its structural symmetry, the boundary conditions are as follows:

$$\begin{cases} \varepsilon_g(L) = \varepsilon_g(-L) = 0 \\ \varepsilon_g(0) = 0\,. \end{cases} \tag{34}$$

Substitute the boundary conditions into Eq. (33), and solve the integral constant to obtain:

$$\varepsilon_g(x) = \varepsilon_m \left[1 - \frac{\cosh(kx)}{\cosh(kL)} \right], \tag{35}$$

where $\varepsilon_g(x)$ is the detection strain of steel wire FBG sensor, that is, the average strain detected by the grating region after the fiber packaging; ε_m is the actual strain of steel wire; and k is the strain lag coefficient determined by the geometric and physical parameters of optical fiber, coating, packaging layer and steel wire.

2.3 STE Coefficient and Minimum Package Length of Optical Fiber

According to Eq. (35), the expression of axial STE coefficient of HSW-FBG sensor is:

$$\phi_{(x)} = \frac{\varepsilon_g(x)}{\varepsilon_m} = 1 - \frac{\cosh(kx)}{\cosh(kL)}\,. \tag{36}$$

From the above equations, the STE coefficient reaches its maximum at the midpoint of the grating and gradually decreases towards both ends. Since the strain detected by the FBG demodulator is the average strain of the grating segment, the required fiber package length can be calculated based on the STE coefficient to be achieved at the grating end. The minimum length of package layer of optical fiber can be obtained from Eq. (36) as follows:

$$L = \frac{1}{k} \cdot \ln \left[\frac{1}{2} \cdot \left(\frac{e^{kx} + e^{-kx}}{1 - \phi_{(x)}} + \sqrt{\left(\frac{e^{kx} + e^{-kx}}{1 - \phi_{(x)}}\right)^2 + 4} \right) \right], \tag{37}$$

which represents the relationship between the half-length of packaging layer L, and the strain lag coefficient k, STE coefficient $\phi_{(x)}$, half-length of the grating x.

In the fabrication of HSW-FBG sensors, the packaging layer thickness typically has dimensions $D_a = 5$ mm in width, $h_a = 1$ mm in upper thickness, and r_a-$r_p = 0.2$ mm in lower thickness. For a standard FBG sensor with a grating length of 10 mm. According to Eq. (37), the STE coefficient reaches 0.9999 when the length of packaging layer is extended to 49.7 mm. This implies near-perfect correspondence between the strain detected by the FBG sensor and the actual strain experienced by the steel wire.

3. Finite Element Simulation

In this section, a three-dimensional finite element (FE) model for the HSW-FBG sensor is developed to determine the optimal parameters for the packaging layer. The impact of geometric and physical parameters of the packaging layer on the STE coefficient is analyzed using the control variable method. Subsequently, the findings are contrasted with the previously established theoretical formula to validate the model's accuracy and effectiveness.

Table 1. Geometric and Physical Parameters of FBG Sensor and Steel Wire

Item	Parameter	Notation	Value	Unit
Optical fiber	Elastic modulus	E_g	7,200	MPa
	Poisson's ratio	λ_g	0.17	/
	Radius	r_g	0.0625	mm
Optical fiber coating	Elastic modulus	E_p	3,000	MPa
	Poisson's ratio	λ_p	0.35	/
	Radius	r_p	0.125	mm
High-strength steel wire	Elastic modulus	E_m	203,000	MPa
	Poisson's ratio	λ_m	0.3	/

Table 2. Initial Values of the Packaging Layer Parameters and Their Ranges

Parameter	Notation	Initial value	Value range	Unit
Elastic modulus	E_a	275	100 – 1,500	MPa
Length	$2L$	50	15 – 60	mm
Upper thickness	h_a	1.0	1 – 6	mm
Poisson's ratio	λ_a	0.4	0.2 – 0.5	/
Width	D_a	5	2 – 6	mm
Lower thickness	$r_a - r_p$	0.2	0.1 – 0.6	mm

3.1 Finite Element Model and Parameters

The High Strength Steel wire under study has a diameter of 7 mm, a length of 500 mm, and exhibits a tensile strength of 1770 MPa. The geometric and physical characteristic parameters of the FBG sensor and high strength steel wire remain constant throughout the analysis, as indicated in Table 1.

To investigate the impact of different materials and packaging dimensions, various parameters related to the packaging layer are considered. The initial values and ranges of these parameters are presented in Table 2. By exploring different combinations within these ranges, the sensitivity of the STE coefficient of the HSW-FBG sensor can be evaluated.

By analyzing various packaging materials, lengths, widths, and upper thicknesses, the aim is to identify the optimal combination of packaging layer parameters that maximizes the STE coefficient for the HSW-FBG sensor. These investigations will provide valuable insights for selecting suitable packaging materials and dimensions to enhance the accuracy and reliability of the strain measurement.

The three-dimensional solid FE models of HSW-FBG sensor comprise high-strength steel wire, packaging layer, optical fiber, and coating layer. To analyze the behavior of the sensor, FE models are created and discretized with hexahedral elements.

The mesh sizes for different components are defined as follows: 1.0 mm for high-strength steel wire, 0.8 mm for packaging layer, and 0.02 mm for optical fiber and coating layer. The FE model is visualized in Fig. 4. In the FE simulation, the boundary condition is applied as follows: one end of the steel wire is fixed while the opposite end is loaded with an axial force of 27,247 N, which corresponds to 0.4 times the tensile strength of the steel wire.

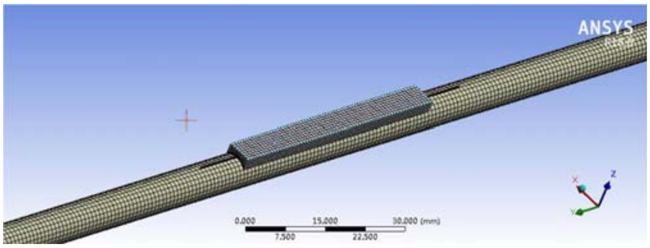

Fig. 4. Finite Element Modeling and Mesh Generation

3.2 Analysis of Influence Parameters

According to the value range of the parameters, multiple values

Table 3. Parameter Values of Packaging Layer

Parameter	Notation	Value	Unit
Elastic modulus	E_a	100, 275, 500, 1000, 1500	MPa
Length	2L	20, 25, 30, 40, 50, 60	mm
Upper thickness	h_a	1, 2, 4, 5	mm
Poisson's ratio	λ_a	0.2, 0.3, 0.4, 0.5	/
Width	D_a	2, 3, 5, 6	mm
Lower thickness	$r_a - r_p$	0.1, 0.2, 0.3, 0.5	mm

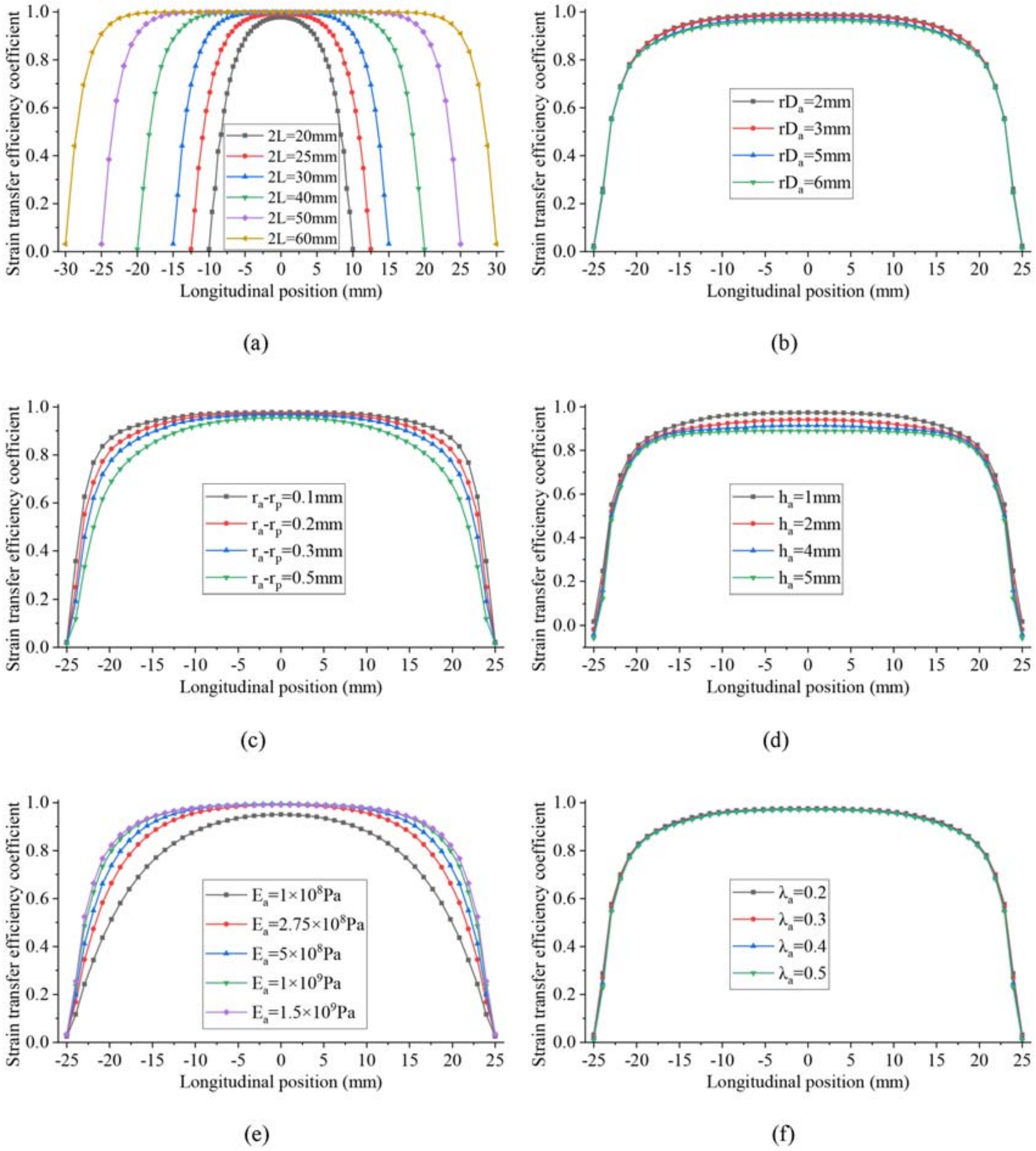

Fig. 5. Longitudinal Distribution of STE Coefficient: (a) Length, (b) Width, (c) Lower Thickness, (d) Upper Thickness, (e) Elastic Modulus, (f) Poisson's Ratio

are selected in each parameter to calculate the STE coefficient, as shown in Table 3. The variability in the STE coefficients under different parameter values can be obtained by finite element model, as shown in Fig. 5.

The STE coefficient reaches its peak value in the middle region of the fiber and decreases rapidly towards the ends. Among the six parameters investigated, the length of the packaging layer exerts the most substantial influence on STE coefficient, while the width and Poisson's ratio exhibit minimal influence. The remaining parameters have a relatively smaller impact. When a sufficiently length of packaging layer, the STE coefficient stabilizes and trends toward 1 in the middle region.

Figure 6 illustrates the comparison between the STE coefficient calculated by the FE model and the theoretical formula. In general, the STE coefficient obtained from the FE simulation is slightly smaller than that obtained from the theoretical formula. This difference can be attributed to the inclusion of shear deformation of the packaging layer and the bending effect induced by the packaging layer on the wire in the FE simulation.

To ensure the necessary measurement accuracy, the STE coefficient should be closely approach 1. The packaging layer's length, which has the most significant impact , should exceed 50 mm, and the elastic modulus should surpass 5 × 10^8 Pa. Other parameters have a minor impact on the STE coefficient and can be determined based on the observed influence trend. For example, a smaller width leads to a larger STE coefficient, so the width should be minimized, ideally around 2 or 3 mm. Similarly, the upper and lower thicknesses should be reduced as much as feasible within the constraints of the packaging process. Poisson's ratio has negligible effect on the STE coefficient.

4. Experimental Investigation

4.1 Orthogonal Experimental Design

The physical parameters and geometric dimensions of the high-strength steel wire and FBG sensor are predetermined and

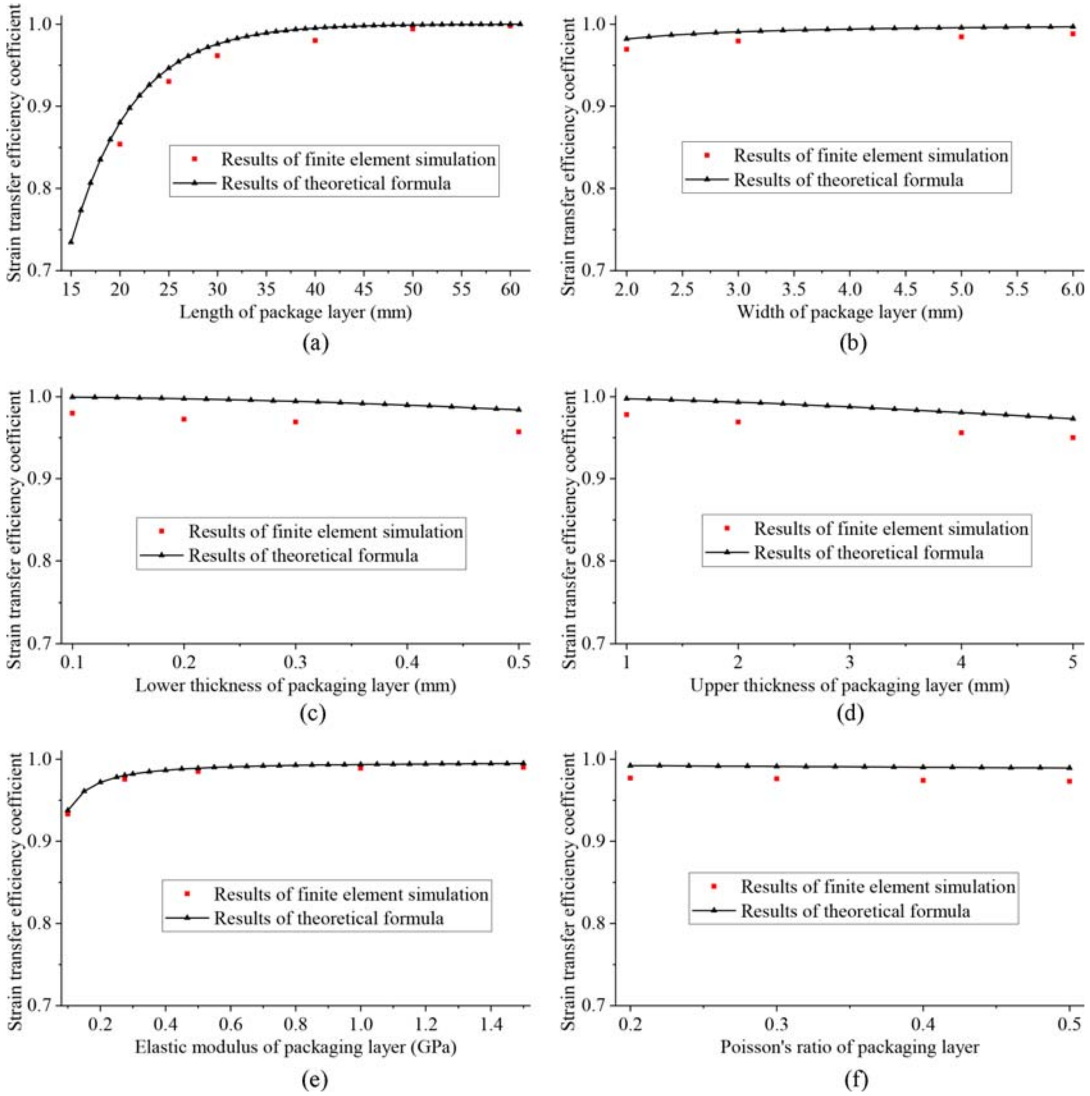

Fig. 6. Comparison of STE Coefficients: (a) Length, (b) Width, (c) Lower Thickness, (d) Upper Thickness, (e) Elastic Modulus, (f) Poisson's Ratio

Table 4. Parameter Design of Orthogonal Experiment

No.	Factors A Length (mm)	 B Width (mm)	 C Upper thickness (mm)	Abbreviation
1	30	3	1	$A_1B_1C_1$
2	30	5	2	$A_1B_2C_2$
3	40	3	2	$A_2B_1C_2$
4	40	5	1	$A_2B_2C_1$
5	50	3	2	$A_3B_1C_2$
6	50	5	1	$A_3B_2C_1$
7	60	3	2	$A_4B_1C_2$
8	60	5	1	$A_4B_2C_1$
9	100	3	2	$A_5B_1C_2$
10	100	5	1	$A_5B_2C_1$

provided in Table 1. Similarly, the physical parameters of the selected structural adhesive, utilized as the packaging layer, are also determined. However, the geometric dimensions of the packaging layer are variable parameters determined during the packaging process of the HSW-FBG sensor. To investigate the influence of these geometric parameters on the optimal combination, an orthogonal experimental design is employed.

In the experiment, the HSW-FBG sensor is fabricated by tightly adhering the optical fiber to the surface of steel wire. Due to the small lower thickness (0.1 – 0.5 mm) of packaging layer, precise measurement becomes challenging. Hence, the lower thickness is excluded from the experiment, resulting in $r_a - r_p = 0$. The orthogonal design consequently concentrates on the length, width, and upper thickness of the packaging layer. Specifically, the length of packaging layer is varied across 30, 40, 50, 60, and 100 mm, the width is chosen as either 3 or 5 mm, and the upper thickness is chosen as either 1 or 2 mm. Through the orthogonal design, ten groups of experimental parameters are selected through the orthogonal design, as presented in Table 4, to thoroughly examine the impact of the packaging layer's geometric parameters on the sensor's performance.

Note that the FBG sensor exhibits high sensitivity to temperature changes, which can necessitate temperature correction for accurate measurement results (Kisala and Cieszczyk, 2015). However, in this context of the current experiment and research, which are conducted exclusively within an indoor laboratory environment with controlled and narrow temperature variation, the influence of temperature on the strain of the FBG sensor is not taken into consideration a significant factor.

4.2 Preparation of Specimens and Experimental Process

The experimental specimens consist of high-strength steel wires with a diameter of 7 mm and a tensile strength of 1,770 MPa. To ensure consistency in the elastic modulus and diameter of the steel wire, all experimental specimens are sourced from the same coil. The packaging layer utilized for the specimens employs a two-component structural adhesive. The cured adhesive exhibits an elastic modulus of $E_a = 2.75 \times 10^8$ Pa and a Poisson's ratio of $\lambda_a = 0.4$. Although the elastic modulus of the cured adhesive is not exceptionally high, it possesses several notable advantages, including excellent impact resistance and fatigue resistance, high peel strength, a wide temperature application range, and an extended curing time that facilitates fabrication process.

The HSW-FBG sensor is fabricated by packaging bare FBG sensor onto the surface of steel wire. The detailed fabrication process is outlined as follows:

1. Surface preparation: polish and wipe the steel wire surface to ensure proper adhesion.
2. Positioning: determine the midpoint of FBG grating region and the desired length of packaging layer.
3. Optical fiber placement: position securely the optical fiber onto the surface at the marked position.
4. Rubber scraper: create a rubber scraper with dimensions corresponding to the desired the width and thickness of the packaging layer.
5. Adhesive application: use the rubber scraper to apply the adhesive uniformly onto the steel wire surface at the marked position.
6. Curing: allow the adhesive to cure for 48 hours.

Figure 7 showcases the experimental specimens of the HSW-FBG sensors. The test of HSW-FBG sensors is conducted using a tensile testing machine. The maximum tensile load applied is set at 30 kN, which corresponds to approximately 0.44 times the load required to reach the tensile strength of the high-strength steel wire. Prior to loading, a preload is applied to

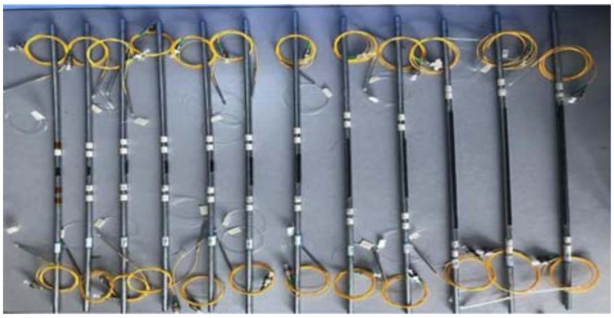

Fig. 7. Experiment Specimens of HSW-FBG Sensor

Fig. 8. Static Tensile Test of HSW-FBG Sensors

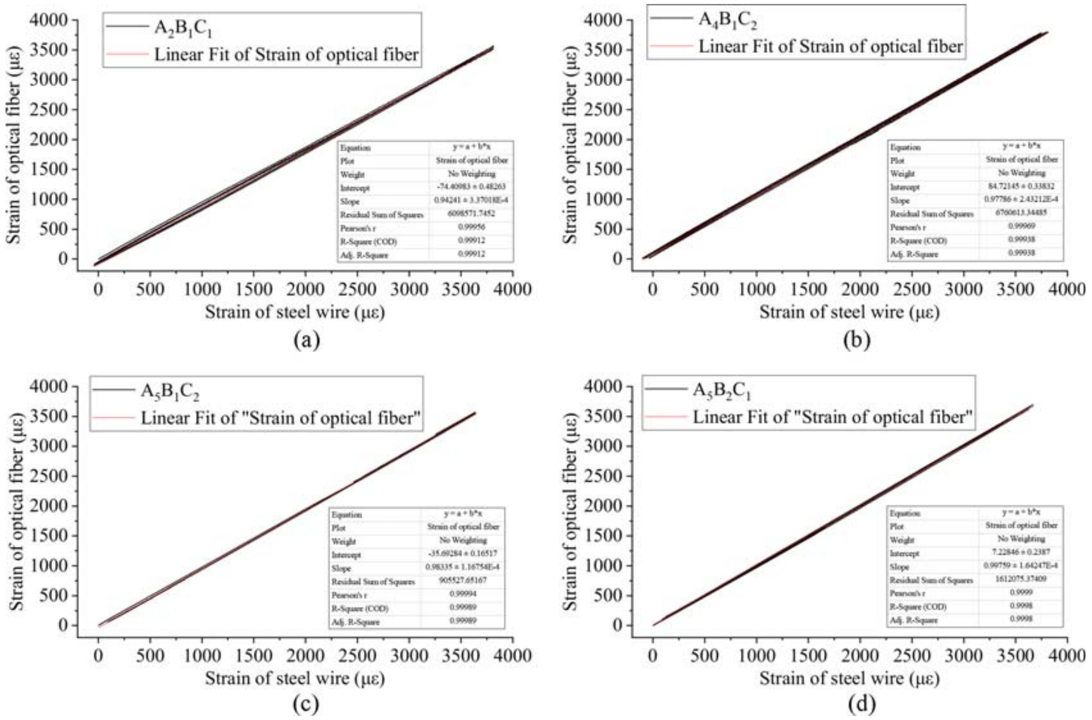

Fig. 9. Fitting Curve of Experimental Results: (a) $A_2B_1C_1$, (b) $A_4B_1C_2$, (c) $A_5B_1C_2$, (d) $A_5B_2C_1$

ensure proper sensor response. The loading process involves linearly increasing the load from 0 to 30 kN at a speed of 1 kN/s. Subsequently, the unloading is performed at the same speed until reaching a load of 1 kN. After unloading, the specimen undergoes three reciprocating loads. The test process is captured in the photographs are depicted in Fig. 8.

During the static tension test, the strain of the steel wire is measured using an electronic extensometer, specifically the YYU-50 model produced by Beijing Iron and Steel Research Institute. Simultaneously, wavelength of the FBG sensor is collected using an FBG demodulator, specifically the HYPERION si155 model produced by MOI (Micron Optics). The data collection frequency for both the electronic extensometer and the FBG demodulator is synchronized at 20 Hz to ensure accurate and concurrent measurements.

4.3 Processing of Experiment Data

The wavelength change of the FBG sensor is converted into the strain of optical fiber using the following calculation formula (Liao et al., 2021):

$$\varepsilon_f = \frac{\Delta\lambda_B}{\lambda_B(1-p_e)}, \tag{38}$$

where ε_f is the strain of optical fiber; $\Delta\lambda_B$ is the wavelength change measured by the FBG sensor; λ_B is the central wavelength of the FBG sensor; and p_e is the effective elastic optical coefficient of the optical fiber.

The effective elastic optical coefficient of the optical fiber is calculated by:

$$p_e = \frac{n_{eff}^2}{2}\left[p_{12} - (p_{11} + p_{12})v\right], \tag{39}$$

where n_{eff} is the effective refractive index of the optical fiber; p_{12} and p_{11} are the elastic constants of the optical fiber, and v is the Poisson's ratio of the optical fiber.

For the pure fused silica FBG sensor used in the experiment, its parameters are (Liao et al., 2021): $p_{11} = 0.121$, $p_{12} = 0.27$, $v = 0.17$, $n_{eff} = 1.456$. The effective elastic optical coefficient can be obtained by substituting the above parameters into Eq. (39): $p_e = 0.2157$.

4.4 Analysis of Experimental Results

4.4.1 Linearity and Repeatability

The strain measured in the high-strength steel wire is linearly fitted to the strain of optical fiber, where the slope of fitting curve representing the STE coefficient of FBG sensor. Fig. 9 illustrates the experimental reciprocating curve and their corresponding linear fitting curve for four different experiment specimens. The determination coefficients (R^2) for linear fitting of the reciprocating curves across all experiments are $R^2 \geq 0.999$, demonstrating excellent linearity and repeatability in the measurements obtained from the HSW-FBG sensor.

In the fabrication process of the 10 experimental specimens, variations in the size of the rubber scraper, adhesive shrinkage, and other factors led to deviations in the actual geometric parameters of the packaging layer compared to the design parameters. Thus, the actual dimensions of each experiment specimen were measured prior to the experiment, as listed in Table 5. The experimentally

Table 5. STE Coefficient of Experiments

Factors		Specimen									
		$A_1B_1C_1$	$A_1B_2C_2$	$A_2B_1C_1$	$A_2B_2C_2$	$A_3B_1C_2$	$A_3B_2C_1$	$A_4B_1C_2$	$A_4B_2C_1$	$A_5B_1C_2$	$A_5B_2C_1$
Geometric parameters	Length (mm)	31	32	42	41	51	52	61	61	101	101
	Width (mm)	2.8	4.9	2.9	5.0	3.1	5.0	2.9	4.9	3.2	4.9
	Upper thickness (mm)	0.98	1.68	1.05	1.62	1.56	1.01	1.75	1.01	0.98	1.66
STE coefficient	Theoretical formula	0.9535	0.9769	0.9893	0.9943	0.9966	0.9990	0.9998	0.9998	0.9999	0.9999
	FE simulation	0.9384	0.9646	0.9671	0.9725	0.9906	0.9968	0.9995	0.9998	0.9999	0.9999
	Experiment	0.8276	0.8915	0.9424	0.9368	0.9665	0.9688	0.9779	0.9797	0.9834	0.9976

obtained STE coefficients of FBG sensor are compared with the results of theoretical formula and FE simulation, as also shown in Table 5.

It can be observed that the STE coefficient derived from theoretical formula is the highest, while the value obtained from the experimental test is the lowest. This discrepancy is likely due to the varying degrees of assumptions made by the three methods; the more assumptions made, the less the results may correspond to the actual physical conditions. Therefore, the experimental test provides the most accurate representation of the STE coefficient of FBG sensor. Additionally, by adjusting the dimensions of the packaging layer are utilized, it is possible to achieve an STE coefficient that is very close to 1, as demonstrated by the coefficient of 0.9976 for the $A_5B_2C_1$ specimen, indicating a high degree of accuracy in strain measurement.

4.4.2 Range of Experimental Results

The influence of length, width, and upper thickness of packaging layer on STE coefficient is examined using the range analysis method. The range of a factor is determined by calculating the maximum difference among all STE coefficients under different levels of that factor. The magnitude of the range indicates the degree of influence of each factor, with a larger range corresponding to a greater impact. To calculate the range of factors in column *j*, the following formula can be applied:

$$R_j = \max\left(\overline{K}_{j1}, \overline{K}_{j2}, \cdots, \overline{K}_{jm}\right) - \min\left(\overline{K}_{j1}, \overline{K}_{j2}, \cdots, \overline{K}_{jm}\right), \quad (40)$$

where R_j is the range of factor; $\overline{K}_{jm}$ is the average value of the sum of experiment indexes corresponding to the level of factor *m* in column *j*.

To evaluate the influence of the length, width, and upper thickness of packaging layer on STE coefficient, the range for each factor is calculated. The factor with the largest range is considered to have the greatest impact on STE coefficient. Two cases are considered:

1. Consistent factor levels: the primary and secondary order can be determined by comparing the size of the range (R) values directly. A larger R indicates a higher degree of influence.
2. Inconsistent factor levels: directly comparing the range (R) values may lead to a larger range for a higher factor level and a smaller range for a lower factor level. To address this, it is necessary to convert the range (R) into coefficients. The conversion formula for the range is as follows:

$$R_j^{'} = d \cdot R_j \sqrt{r}, \quad (41)$$

where $R_j^{'}$ is the converted range; *r* is the number of experimental repetitions for each factor; and *d* is the conversion coefficient, which is 0.71 when $r = 2$, and is 0.4 when $r = 5$.

Table 6. Range of Experimental Results

No.	Factors		
	Length	Width	Upper thickness
K_{j1}	1.7191	4.6978	4.6963
K_{j2}	1.8792	4.7744	4.7617
K_{j3}	1.9353		
K_{j4}	1.9576		
K_{j5}	1.9810		
$\overline{K}_{j1}$	0.8596	0.9396	0.9393
$\overline{K}_{j2}$	0.9396	0.9549	0.9523
$\overline{K}_{j3}$	0.9677		
$\overline{K}_{j4}$	0.9788		
$\overline{K}_{j5}$	0.9905		
R_j	0.1309	0.0153	0.013
R'_j	0.0740	0.0243	0.0206

According to the experiment results in Table 5, the range analysis for the three factors affecting STE coefficient is summarized in Table 6. The converted range $R_j^{'}$ for length, width, and upper thickness of packaging layer are calculated as 0.0740, 0.0243, and 0.0206, respectively. Therefore, the sequence of influencing factors, in descending order of significance, is length, width, and upper thickness. Notably, the length has a significantly greater influence on the STE coefficient than either the width or the upper thickness.

The optimal combination is achieved when the packaging layer parameters result in an STE coefficient that is as close to 1 as possible. The analysis indicates that the optimal combinations are $A_4B_1C_2$, $A_4B_2C_1$, $A_5B_1C_2$, $A_5B_2C_1$. Although the width and upper thickness values in $A_5B_1C_2$ not being at their optimal levels, the primary influencing factor — the length — is at an optimal level, which is sufficient to drive the STE coefficient to approach 1. This underscores the importance of the length of the packaging layer in achieving a high STE coefficient and, consequently, accurate strain measurement.

5. Comparison and Analysis

The STE coefficient of each experimental specimen is shown in Fig. 10, considering two different widths of the packaging layer, namely 3 and 5 mm. When the length of packaging layer falls within the range of 30 to 52 mm, there is a noticeable difference in STE coefficient depending on the width of packaging layer. Specifically, a wider packaging layer results in a higher STE coefficient. This discrepancy occurs because, at smaller packaging layer lengths, the width of packaging layer has a greater influence on STE coefficient compared to the upper thickness of the packaging layer, which has a minimal impact.

The actual parameter values of each experimental specimen are substituted into the theoretical formula and the FE model to calculate the STE coefficient. These calculated values are then compared with the results from the orthogonal experiments, as shown in Fig. 11. Within the range of 30 to 50 mm for the length of packaging layer, the theoretical value of the STE coefficient is found to be the highest, followed by the FE value, and then the experimental value. This comparison can be attributed to two reasons. Firstly, the theoretical formula does not consider the shear deformation of packaging layer. Secondly, in the FE simulation and theoretical calculation, although the geometric parameters of packaging layer are consistent with the actual values, there might be certain errors in the values of physical parameters that affect the overall accuracy of the calculations.

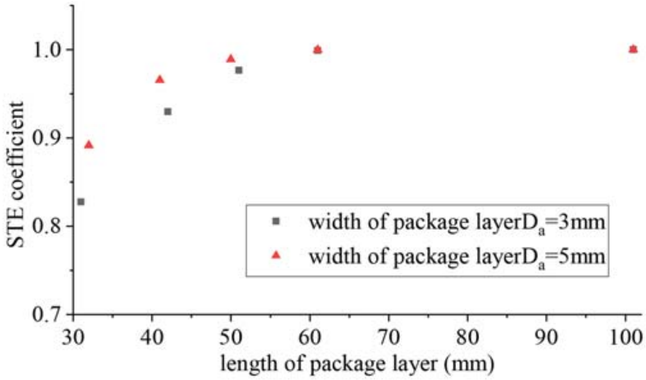

Fig. 10. Comparison of STE Coefficients with Different Packaging Layer Widths

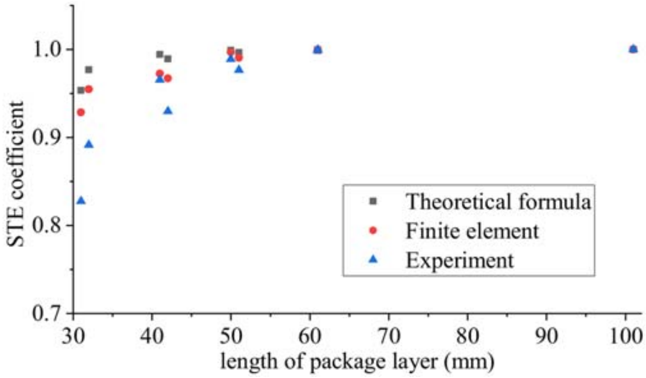

Fig. 11. Comparison of STE Coefficient Obtained by Different Methods

However, when the length of packaging layer is increased to between 60 and 100 mm, the STE coefficients calculated by all three methods are nearly equal and very close to 1. During this range, the length of the packaging layer becomes the dominant factor influencing the STE coefficient, while the influence of other geometric and physical property parameter errors can be neglected.

The STE coefficient of HSW-FBG sensor is determined through a combination of theoretical formulas, FE simulations, and static tensile tests. Comparative analysis demonstrates that a shorter packaging length does not guarantee a higher STE coefficient for the FBG sensor, nor does it ensure consistency in the STE coefficient under identical packaging parameters. Conversely, when the length of packaging layer is equal to or greater than 60 mm, the STE coefficient of the FBG sensor approaches 1 and is insensitive to variations in the other geometric parameters of the packaging layer.

This is due to the fact that when the steel wire experiences strain, the packaging layer transfers this strain to the fiber through shear deformation, which is then sensed and measured by the fiber grating. In this process of strain transfer, the shear deformation of the encapsulation layer is primarily caused by the significant strain gradient at both ends of the encapsulation layer. However, the area with a large strain gradient is not extensive, as can be observed from the distribution diagram of the strain transfer efficiency along the longitudinal wire in the finite element simulation, as depicted in Fig. 5. Additionally, since the length of the strain-sensing grating is only 5 – 10 mm, as long as the packaging layer is sufficiently long, the strain of the grating will not be significantly affected by the shear deformation of the packaging layer. Consequently, the strain transfer coefficient of the fiber grating approaches 1. This has been verified through theoretical formula calculations, finite element simulations, and experimental measurements.

Based on the optimal combination of geometric parameters for packaging layer and considering practical packaging operations, it is recommended to use a packaging layer with dimensions of 100 mm to 200 mm in length, 5 mm in width, and 1 mm in upper thickness. This recommendation ensures that the packaging layer is sufficiently long to minimize the impact of shear deformation on the grating's strain, while also considering the ease of packaging and handling during fabrication.

6. Conclusions

1. A four-layer structure model is proposed to simplify the analysis of the HSW-FBG sensor. Based on the shear-lag theory, formulas for the STE coefficient between the measured strain and the actual strain of the HSW-FBG sensor are derived. Additionally, a formula for determining the minimum required

length of the packaging layer is obtained, providing theoretical guidance for the precise fabrication of similar sensors.

2. The bare FBG sensor is successfully packaged on the high-strength steel wire using a two-component structural adhesive, with the detailed packaging process outlined to facilitate a straightforward and efficient fabrication. The HSW-FBG sensor exhibits excellent linearity and repeatability in strain detection.
3. Through analysis of FE model parameters and results from orthogonal experiments, it is determined that the length of the packaging layer is the primary factor affecting the STE coefficient, while the other parameters have a relatively minor impact.
4. A comparison of theoretical formulas, FE simulations, and experimental results reveals that when the length of the packaging layer is not less than 60 mm, the STE coefficient of the HSW-FBG sensor closely approaches 1, demonstrating high-precision measurement of cable force without the necessity for strain correction.

In general, the STE coefficient is a significant parameter for packaged FBG sensors, and the proposed HSW-FBG sensor with its large slenderness ratio can achieve a STE coefficient close to 1 by utilizing conventional adhesive and appropriate packaging length. The packaging process is straightforward and easy to implement, and the analysis and verification of the STE coefficient in the HSW-FBG sensor offer a foundation for long-term stress monitoring of cable wires. Also, it provides insights into the packaging method and accuracy analysis for similar sensors. With a comprehensive study on the static performance of the HSW-FBG sensor, particularly its strain transfer efficiency coefficient, the significant capabilities of this sensor in monitoring the axial force of bridge cables have been demonstrated. The subsequent research will involve an analysis and verification of its temperature characteristics, durability, and other aspects, aiming to establish a robust foundation for the engineering application of the HSW-FBG sensor.

Acknowledgments

The authors would like to appreciate the support of the National Key R&D Program of China (2023YFB2604400), the Guangdong Basic and Applied Basic Research Foundation under Grant 2020A1515110240, the Sichuan Science and Technology Program under Grant 2023NSFSC0891, and the National Natural Science Foundation of China under Grant 52208209.

ORCID

Kun Yan https://orcid.org/0009-0005-1673-2622
Lu Wang https://orcid.org/0000-0001-5051-4059

References

Ansari F, Libo Y (1998) Mechanics of bond and interface shear transfer in optical fiber sensors. *Journal of Engineering Mechanics* 124(4): 385-394, DOI: 10.1061/(ASCE)0733-9399(1998)124:4(385)

Bonopera M (2022) Fiber-bragg-grating-based displacement sensors: Review of recent advances. *Materials (Basel, Switzerland)* 15(16), DOI: 10.3390/ma15165561

Camassa D, Castellano A, Fraddosio A, Miglionico G, Piccioni MD (2021) Dynamic identification of tensile force in tie-rods by interferometric radar measurements. *Applied Sciences* 11(8):3687, DOI: 10.3390/app11083687

Chen W, Wu J, Zhang P, Liu L, Liu H (2012) Metallized bonding technology of fiber bragg grating strain sensor. *Sensor Letters* 10(7):1474-1477, DOI: 10.1166/sl.2012.2472

Di Sante R, Donati L, Troiani E, Proli P (2014) Reliability and accuracy of embedded fiber Bragg grating sensors for strain monitoring in advanced composite structures. *Metals and Materials International* 20(3):537-543, DOI: 10.1007/s12540-014-3020-7

Hill KO, Fujii Y, Johnson DC, Kawasaki BS (1978) Photosensitivity in optical fiber waveguides: Application to reflection filter fabrication. *Applied Physics Letters* 32(10), DOI: 10.1063/1.89881

Hou G, Li Z, Wang K, Hu J (2021) Structural deformation sensing based on distributed optical fiber monitoring technology and neural Network. *KSCE Journal of Civil Engineering* 25(11):4304-4313, DOI: 10.1007/s12205-021-1805-z

Im J, Kim M, Choi KS, Hwang TK, Kwon IB (2014) Aluminum-thin-film packaged fiber Bragg grating probes for monitoring the maximum tensile strain of composite materials. *Applied Optics* 53(17):3615-20, DOI: 10.1364/AO.53.003615

Jo HC, Kim SH, Lee J, Sohn H, Lim YM (2021) Sag-based cable tension force evaluation of cable-stayed bridges using multiple digital images. *Measurement* 186:110053, DOI: 10.1016/j.measurement.2021.110053

Kalamkarov AL, Fitzgerald SB, Macdonald DO, Georgiades AV (2000) The mechanical performance of pultruded composite rods with embedded fiber-optic sensors. *Composites Science & Technology* 60(8):1161-1169, DOI: 10.1016/S0266-3538(00)00021-X

Kangas S, Helmicki A, Hunt V, Sexton R, Swanson J (2012) Cable-stayed bridges: Case study for ambient vibration-based cable tension estimation. *Journal of Bridge Engineering* 17(6):839-846, DOI: 10.1061/(ASCE)BE.1943-5592.0000364

Kisala P, Cieszczyk S (2015) Method of simultaneous measurement of two direction force and temperature using FBG sensor head. *Applied Optics* 54(10):2677-87, DOI: 10.1364/AO.54.002677

Kulpa M, Howiacki T, Wiater A, Siwowski T, Sieńko R (2021) Strain and displacement measurement based on distributed fibre optic sensing (DFOS) system integrated with FRP composite sandwich panel. *Measurement* 175:109099, DOI: 10.1016/j.measurement.2021.109099

Li H, Ou J, Zhou Z (2009) Applications of optical fibre Bragg gratings sensing technology-based smart stay cables. *Optics and Lasers in Engineering* 47(10):1077-1084, DOI: 10.1016/j.optlaseng.2009.04.016

Li D, Zhou Z, Ou J (2011) Development and sensing properties study of FRP-FBG smart stay cable for bridge health monitoring applications. *Measurement* 44(4):722-729, DOI: 10.1016/j.measurement.2011.01.005

Li H, Zhou G, Ren L (2007) Strain transfer model of fiber sensors under non-axial stress. *Acta Optica Sinica* (5):787-793, DOI: 10.3321/j.issn:0253-2239.2007.05.007 (in Chinese)

Liao YB, Li M, Xia L (2021) Fiber optics (3rd Edition). Tsinghua University Press, China, 299-305 (in Chinese)

Liu LH, Zhao X, Li S, Zhou ZB, Jiang DS (2010) Smart bridge cable integrated with fiber bragg grating sensors. *Journal of Highway and Transportation Research and Development* 27(12):67-71+93, DOI: 10.3969/j.issn.1002-0268.2010.12.013 (in Chinese)

Mahakud R, Kumar J, Prakash O, Dixit SK (2013) Study of the nonuniform behavior of temperature sensitivity in bare and embedded fiber Bragg gratings: Experimental results and analysis. *Applied Optics* 52(31):7570-9, DOI: 10.1364/AO.52.007570

Majumder M, Gangopadhyay TK, Chakraborty AK, Dasgupta K, Bhattacharya DK (2008) Fibre Bragg gratings in structural health monitoring—Present status and applications. *Sensors and Actuators A: Physical* 147(1):150-164, DOI: 10.1016/j.sna.2008.04.008

Mehrabi AB, Farhangdoust S (2018) A laser-based noncontact vibration technique for health monitoring of structural cables: Background, success, and new developments. *Advances in Acoustics and Vibration* 2018:1-13, DOI: 10.1155/2018/8640674

Mueller UC, Zeh T, Koch AW, Baier H (2006) Fiber optic bragg grating sensors for high-precision structural deformation control in optical systems. *Proceedings of SPIE - The International Society for Optical Engineering* 6167:61670A-61670A-12, DOI: 10.1117/12.668039

Ren L, Jia Z, Li H, Song G (2014) Design and experimental study on FBG hoop-strain sensor in pipeline monitoring. *Optical Fiber Technology* 20(1):15-23, DOI: 10.1016/j.yofte.2013.11.004

Sahota JK, Gupta N, Dhawan D (2020) Fiber Bragg grating sensors for monitoring of physical parameters: A comprehensive review. *Optical Engineering* 59(6):060901-060935, DOI: 10.1117/1.OE.59.6.060901

Salo J, Korhonen I (2014) Calculated estimate of FBG sensor's suitability for beam vibration and strain measuring. *Measurement* 47:178-183, DOI: 10.1016/j.measurement.2013.08.017

Torres B, Payá-Zaforteza I, Calderón PA, Adam JM (2011) Analysis of the strain transfer in a new FBG sensor for Structural Health Monitoring. *Engineering Structures* 33(2):539-548, DOI: 10.1016/j.engstruct.2010.11.012

Vosoughifar H, Khorani M (2019) Optimal sensor placement of RCC dams using modified approach of COMAC-TTFD. *KSCE Journal of Civil Engineering* 23(7):2933-2947, DOI: 10.1007/s12205-019-0716-8

Wang ML, Satpathi D, Koontz S, Jarosevic A, Chandoga M (1999) Monitoring of cable forces using magneto-elastic sensors. *Computational Mechanics in Structural Engineering*, 337-347, DOI: 10.1016/B978-008043008-9/50064-8

Wang L, Shen RL, Zhang SH, Bai LH, Zhen XX, Wang RH (2021a) Strand element analysis method for interaction between cable and saddle in suspension bridges. *Engineering Structures* 242:112283, DOI: 10.1016/j.engstruct.2021.112283

Wang Z, Zhou Z, Ji J, Zhao J, Zhao X, Qiang Q, Wu Q (2021b) Application of smart cables with fiber bragg grating sensors to super large bridge. *Metal Products* 47(1):59-64, DOI: 10.3969/j.issn.1003-4226.2021.01.015 (in Chinese)

Weng JH, Chen L, Sun LM, Zou YQ, Liu ZH, Guo H (2023) Fully automated and non-contact force identification of bridge cables using microwave remote sensing. *Measurement* 209:112508, DOI: 10.1016/j.measurement.2023.112508

Wu B, Zhou Y, Lu H, Huang Y, Zhou Z (2022) Fatigue resistance of a BFRP-encapsulated long-gauge FBG strain sensor under cyclic train loads. *KSCE Journal of Civil Engineering* 26(9):3945-3953, DOI: 10.1007/s12205-022-1355-z

Wu J, Chen W, Liu L, Zhao X, Liu L, Liu H (2012) A novel cable tension monitoring method based on self stress attenuation feature in cable anchor head. *Sensor Letters* 10(7):1364-1367, DOI: 10.1166/sl.2012.2471

Yao Y, Yan M, Bao Y (2021) Measurement of cable forces for automated monitoring of engineering structures using fiber optic sensors: A review. *Automation in Construction* 126:103687, DOI: 10.1016/j.autcon.2021.103687

Yashiro S, Okabe T, Toyama N, Takeda N (2007) Monitoring damage in holed CFRP laminates using embedded chirped FBG sensors. *International Journal of Solids and Structures* 44(2):603-613, DOI: 10.1016/j.ijsolstr.2006.05.004

Yun C, Min J (2011) Smart sensing, monitoring, and damage detection for civil infrastructures. *KSCE Journal of Civil Engineering* 15(1):1-14, DOI: 10.1007/s12205-011-0001-y

Zeng P, Wang Y, Chen F, Sun Y, Zhang Q, Huang X, You Z (2019) Analysis of the effect of adhesives on strain transfer for surface bonded polyimide fiber bragg grating. *Chinese Journal of Sensors and Actuators* 32(1):43-49, DOI: 10.3969/j.issn.1004-1699.2019.01.008 (in Chinese)

Zhang Y, Zhu L, Luo F, Dong M, Yang R, He W, Lou X (2016) Comparison of metal-packaged and adhesive-packaged fiber bragg grating sensors. *IEEE Sensors Journal* 16(15):5958-5963, DOI: 10.1109/JSEN.2016.2577610

Zhao X, Liu L, Ji J, Zhang E, Xue H, Zhou Z (2013) Application of intelligent cable in siyang bridge of beijing-hangzhou canal. *Journal of China and Foreign Highway* 33(2):92-96, DOI: 10.3969/j.issn.1671-2579.2013.02.024 (in Chinese)

Zhou Y, Huang Z, Wang Y, Xiang Z, Zhou J, Zhang X (2021) Measurement method of stay cable force based on measured cable shape using laser scanning. *China Journal of Highway and Transport* 34(12):91-103, DOI: 10.19721/j.cnki.1001-7372.2021.12.008 (in Chinese)